NEUROSCIENCE

Iron is neurotoxic in retinal detachment and transferrin confers neuroprotection

Alejandra Daruich[1,2,3], Quentin Le Rouzic[1], Laurent Jonet[1], Marie-Christine Naud[1], Laura Kowalczuk[2], Jean-Antoine Pournaras[2], Jeffrey H. Boatright[4,5], Aurélien Thomas[6,7], Natacha Turck[7,8], Alexandre Moulin[2], Francine Behar-Cohen[1,7,9]*†, Emilie Picard[1]*

In retinal detachment (RD), photoreceptor death and permanent vision loss are caused by neurosensory retina separating from the retinal pigment epithelium because of subretinal fluid (SRF), and successful surgical reattachment is not predictive of total visual recovery. As retinal iron overload exacerbates cell death in retinal diseases, we assessed iron as a predictive marker and therapeutic target for RD. In the vitreous and SRF from patients with RD, we measured increased iron and transferrin (TF) saturation that is correlated with poor visual recovery. In ex vivo and in vivo RD models, iron induces immediate necrosis and delayed apoptosis. We demonstrate that TF decreases both apoptosis and necroptosis induced by RD, and using RNA sequencing, pathways mediating the neuroprotective effects of TF are identified. Since toxic iron accumulates in RD, we propose TF supplementation as an adjunctive therapy to surgery for improving the visual outcomes of patients with RD.

INTRODUCTION

Retinal detachment (RD) is an ocular emergency, as separation of the neuroretina from the underlying retinal pigment epithelium (RPE) (Fig. 1A, arrowhead) disturbs photoreceptor (PR) metabolism, causing PR death and subsequent vision loss (*1*). In rhegmatogenous retinal detachment (RRD), a retinal tear (Fig. 1A, arrowhead) induces subretinal fluid (SRF) accumulation in a space formed between the neuroretina and the RPE. The incidence of adult RRD varies between 10 and 55 per 100,000 individuals per year, with higher occurrence in patients who also have myopia or pseudophakia (*2*). This incidence will likely rise with myopia increasing worldwide (*3*). Intraocular surgery is commonly used to repair RRD but must be realized rapidly after detachment, as the duration of macular detachment is one of the major visual prognosis factors (*4*). The principles of surgery are based on retinal break closure (i.e., by laser therapy or cryotherapy) and internal or external temporary tamponade to maintain the retina attached during wound healing. When the procedure is performed internally, vitreous is removed and SRF is eventually extracted. Despite tremendous progress made in surgical techniques and the high repair rate, 60% of patients with RRD involving the macula (macula-OFF RD, 50% of the cases) recover less than 20/40 vision (*4*) and have poor vision-related quality of life (*5*). Improving vision after RD surgery is thus a critical therapeutic challenge.

Experimental models of RD correlate well with human pathology, making them appropriate to study mechanisms and pharmacotherapeutic strategies. First changes are observed at the RPE/PR interface (*6*), followed by PR cell death that peaks at 2 to 3 days through apoptosis, necrosis, and autophagic cell death mechanisms (*1*). Caspase inhibitors do not prevent cell death in RRD models but rather promote receptor-interacting protein (RIP) kinase–dependent necrosis, referred to as necroptosis (*7*). Subsequent inflammatory reactions, including macrophage/microglial activation, contribute to a neurotoxic environment and to subsequent gliosis (*8*). Factors initiating cell death during RD remain undetermined, and the identification of a common target of the different death mechanisms is mandatory for developing an effective neuroprotective strategy for RD.

Iron is an important biological component for catalyzing enzymatic reactions, but when it is poorly liganded, iron generates reactive oxygen species, damaging cellular components (*9*). Iron-mediated retinal cell death has been suspected to occur in various forms of retinal degeneration (*10*), including age-related macular degeneration (AMD) (*10*), the leading cause of blindness in developed countries, but no correlation between iron and visual function was possible, and the iron sequestration capacity in human ocular fluids has never been evaluated in relation to retinal diseases. The control of ocular iron homeostasis is tightly controlled by retinal cell proteins, and the iron transporter, transferrin (TF), is one major protein found in the vitreous. We previously showed that the sequestration of two ferric iron ions by TF (*11*) prevents the formation of free radical–mediated stress and glial retinal cell death in culture. Our previous studies also showed, in various animal models, that treatment with TF exerted retinal neuroprotective effects through the reduction of apoptosis, inflammation, and oxidative stress (*12*, *13*). However, the molecular mediators and pathways involved in the protective effects of TF have never been investigated in depth.

In our study, we evaluated the iron and TF status in ocular fluids from patients with RRD and correlated those parameters to visual acuity recovery and duration of RRD. Retinal explants are a common tool used for RD studies, recapitulating pathological processes found in the detached retina (*14*). Thus, we established an ex vivo model of RRD by placing rodent retinas under iron overload culture conditions and investigated whether TF protects the retina by evaluating apoptosis, necroptosis, and oxidative stress cell markers.

[1]INSERM, UMRS1138, Team 17, From physiopathology of ocular diseases to clinical development, Université Sorbonne Paris Cité, Centre de Recherche des Cordeliers, 15 rue de l'Ecole de Médecine, 75006 Paris, France. [2]Department of ophthalmology, University of Lausanne, Jules-Gonin Eye Hospital, Fondation Asile des Aveugles, Lausanne, Switzerland. [3]Ophthalmology Department, Necker-Enfants Malades University Hospital, AP-HP, Paris, France. [4]Department of Ophthalmology, School of Medicine, Emory University, Atlanta, GA, USA. [5]Center of Excellence, Atlanta Veterans Administration Medical Center, Decatur, GA, USA. [6]Geneva University Hospitals, Unit of Toxicology, CURML, Geneva, Switzerland. [7]Faculty of Biology and Medicine, University of Lausanne, Rue du Bugnon 21, 1011 Lausanne, Switzerland. [8]Geneva University, Department of Human Protein Science, Geneva, Switzerland. [9]Ophtalmopole, Cochin Hospital, AP-HP, Assistance Publique Hôpitaux de Paris, 24 rue du Faubourg Saint-Jacques, 75014 Paris, France.
*These authors contributed equally to this work.
†Corresponding author. Email: francine.behar@gmail.com

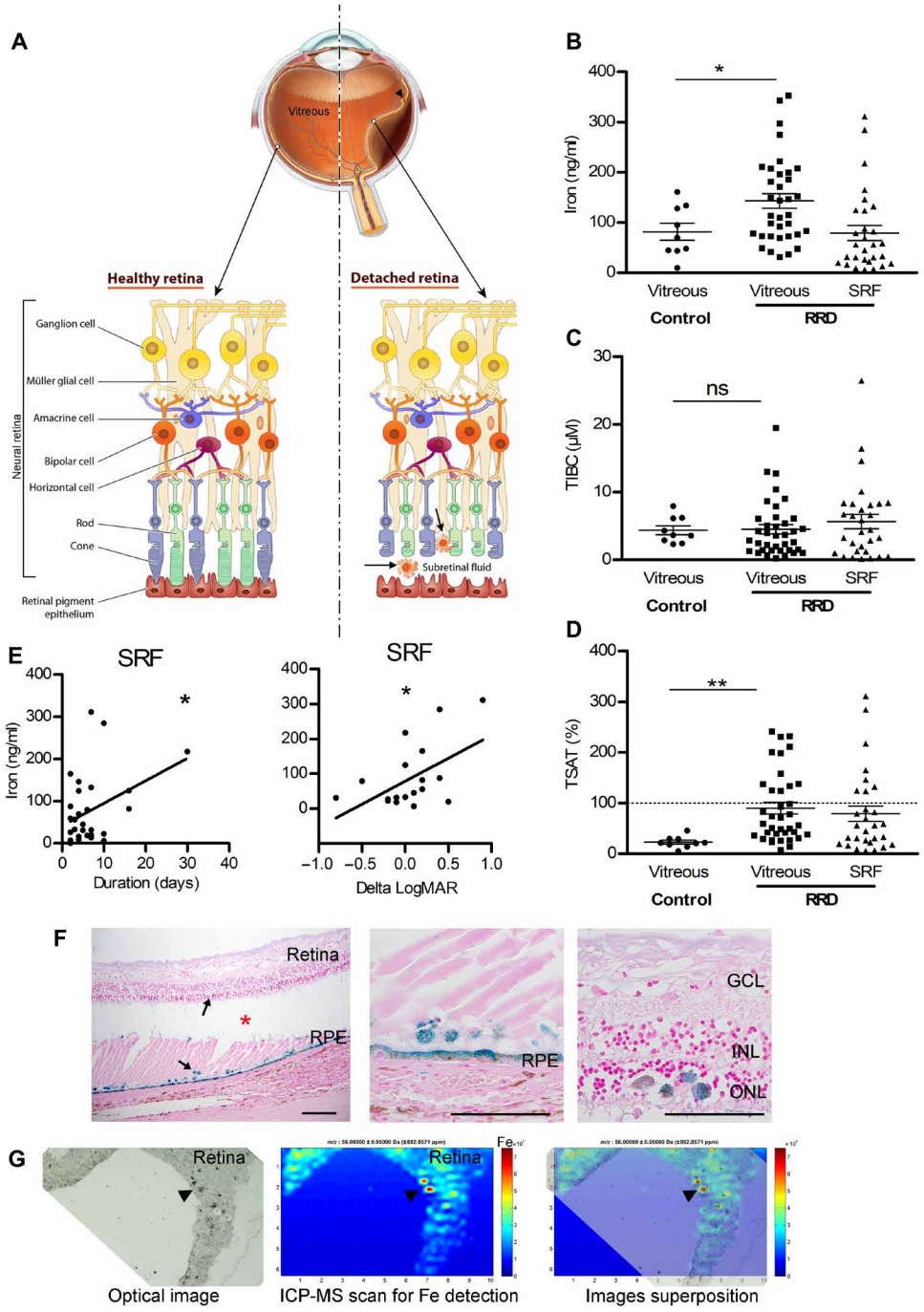

Fig. 1. Iron accumulates during RD in humans. (**A**) Schematic representation of RRD. RPE strictly interacted with PRs (rods and cones), supporting their function and maintaining retinal physiology. During RRD, separation of the neural retina from the RPE disrupts the metabolism of PRs and induces permanent cellular damage, SRF accumulation through the retinal tear (arrowhead), and inflammatory cells in subretinal space. (**B** to **D**) Iron level (B), total iron binding capacity (TIBC) (C), and transferrin saturation (TSAT) (D) were quantified in vitreous from control patients and in vitreous and SRF from patients with RRD. Unpaired *t* test ($n = 9$ to 35 for vitreous and $n = 30$ for SRF), $^{*}P = 0.046$ and $^{**}P = 0.006$. ns, not significant. (**E**) Iron level in SRF was correlated to duration of the RRD ($n = 30$) and to the visual recovery 1 month following surgical treatment ($n = 10$). Pearson correlation test, $^{*}P < 0.05$. (**F**) Perl's staining (blue) on retinal sections from patients with nonhemorrhagic RD (asterisk shows space between retina and underlying RPE) revealed iron deposits in the retina and the RPE (arrows). Scale bars, 500 µm. (**G**) Iron distribution map realized by inductively coupled plasma mass spectrometry (ICP-MS) on the retina from a patient with nonhemorrhagic RD revealed iron deposits (arrowheads). An optical image of the analyzed retina section (left), the corresponding ICP-MS image of Fe distribution (medium), and the superposition of both (right). The color spectrum represents an ion intensity map of Fe. GCL, ganglion cell layer; INL, inner nuclear layer; ONL, outer nuclear layer; *m/z*, mass/charge ratio; ppm, parts per million. All values are represented as the mean ± SEM.

Transgenic mice expressing human TF (hTF) in the retina were used to observe TF neuroprotective efficiency in an experimentally induced RD model (*15*), and an RNA sequencing (RNA-seq) approach was used to explore the pathways implied in these effects. Intravitreal injection of TF in rats following experimental RD was used to determine the potential of TF as an adjuvant for RD surgery.

RESULTS

In ocular fluids from patients with RRD, iron increases with detachment duration and correlates with poor visual recovery

Total iron, TF, total iron binding capacity (TIBC), and percentage of transferrin saturation (TSAT) were evaluated in undiluted vitreous and SRF collected from patients with RRD (age, 64.3 years; SD, 9.6; 11 females and 24 males; $n = 35$) and from control patients (age, 70.2 years; SD, 9.5; 5 females and 4 males; $n = 9$). In the vitreous, the level of iron was significantly higher in patients with RRD as compared to control subjects without RD (143.1 ± 14.4 ng/ml versus 81.7 ± 16.8 ng/ml; $P = 0.046$) (Fig. 1B). The TIBC values did not differ in eyes with or without RRD (4.5 ± 0.7 and 4.3 ± 0.6 μM TF; $P > 0.5$), but TSAT increased from 22.8 ± 3.8% in control eyes to 89.91 ± 11.4% in eyes with RRD, reaching almost complete saturation ($P = 0.006$; Fig. 1, C and D). In the SRF, the high rate of TSAT (53.5 ± 12.6%) (Fig. 1D) also reflected iron overload. Higher levels of iron in the SRF were associated with longer duration of detachment ($P = 0.038$; Fig. 1E, left graph) and correlated with lower visual recovery 1 month after surgery ($P = 0.047$; Fig. 1E, right graph). Because the data are correlative, these results suggest that iron toxicity could contribute to the functional outcome in RRD.

Iron deposits, evaluated in postmortem ocular tissue sections of RD, were found in the remaining PR layer, inside cells in the subretinal space that are very likely to be inflammatory cells (arrows), and in RPE (Fig. 1F) using Perl's staining. Inductively coupled plasma mass spectrometry (ICP-MS) analysis confirmed elevated iron content throughout the retina sections (Fig. 1G, green), with higher concentrations in focal areas (red, arrowheads). These observations suggest that iron could mediate, at least partially, PR damage during RRD.

Iron induces PR death in rat retinal explants ex vivo

To evaluate iron neurotoxicity, rat neural retina explants were cultured in low-serum medium, and PR cells were immediately exposed to iron at a range of concentrations similar to those measured in SRF from patients with RRD. After 2 days of exposure to 1 mM $FeSO_4$ (fig. S1A), no increase in caspase-dependent apoptosis was observed [caspase 3 activation and TUNEL (terminal deoxynucleotidyl transferase–mediated deoxyuridine triphosphate nick end labeling)–positive cells were similar under control and iron conditions] (fig. S1, B and C). However, lactate dehydrogenase (LDH) release, an early marker of necrosis, was concentration-dependently increased as early as 1 day after iron overload exposure (fig. S1D). After 2 days of iron overload, necroptosis was confirmed with an increase of RIP kinase protein expression and staining of PR nuclei with propidium iodide (fig. S1, E and F). The 2 days of iron exposure led to the loss of both rod and cone PRs, as shown by the decreased rhodopsin protein level with increasing concentration of $FeSO_4$ (Fig. 2B) and nearly no arrestin-positive cones remaining after 1 mM $FeSO_4$ exposure (Fig. 2C, arrows). After iron overload, progressive histological damage appeared over time, leading to complete retinal layer disorganization and shortening of the residual PR segments (Fig. 2D), iron diffusely stained the retinal explants 7 days after iron removal, particularly in the remaining PR segments, and was concentrated in inflammatory cell types (brown, arrows), as observed in human RD sections (Fig. 2E). The direct contact of iron with PR led to immediate necroptosis that increased with higher iron concentrations and with longer iron exposure times.

TF protects against iron-induced toxicity in ex vivo mouse and rat retinal explants

In transgenic (TG) mice expressing hTF in retinal cells (*11*), hTF levels increased in the medium with the duration of retinal explant culture (fig. S2, A to C). TG-derived explants exhibited fewer signs of degeneration and oxidative stress in low-serum medium compared with wild-type (WT) explants. After 6 days of culture, retinal glial Müller cell activation, identified by glial fibrillary acidic protein (GFAP) distribution (fig. S2D, arrow) (*16*), and markers of oxidative stress [8-hydroxyguanosine (8-HGN) and 4-hydroxynonenal (4-HNE)] (fig. S2, E and F) were reduced in retinal explants from TG mice compared with those from WT mice.

Subsequently, we investigated whether TF was protective against iron overload combined with RD. Iron overload conditions were applied to TG and WT retinal explants (Fig. 3A). LDH release, evaluated after 1 day, was reduced by 24.4% in retinal explants from TG mice as compared with explants from WT mice ($P = 0.03$; Fig. 3B). After 6 days of iron exposure, the number of cones was 55.5% higher and the outer segment (OS) lengths were 58.2% longer in retinas from TG mice as compared with WT ($P < 0.0001$ for both; Fig. 3C). In addition, reduced Müller glial cell activation and oxidative stress markers (fig. S3, A to C) were observed in retinal explants from TG mice. The expression of hTF in TG mice retinas reduced iron accumulation as indicated by a reduction in ferritin light chain (LFt) staining (Fig. 3D) (*12*). The TG mouse retinas were thus protected from iron-induced oxidative stress and necroptosis.

We then evaluated the effect of TF added to rat retinal explants after 2 days of iron exposure to more closely mimic the therapeutic time course common in human RD treatment. After 2 days, iron was removed and exogenous hTF (50 mg/ml) was added in the medium (Fig. 3E). TF treatment rescued not only rod-specific protein [61.7% greater rhodopsin level ($P = 0.021$); Fig. 3F] and the lengths of rod OSs (Fig. 3G, asterisk) but also cones [83.8% greater number of cones versus untreated ($P = 0.04$); Fig. 3G, arrows]. Two days after iron exposure, the RIP kinase protein level remained elevated, but the presence of the cleaved form of RIP kinase proteins (Fig. 3H) suggested an activation of caspase 8, leading to a delayed activation of apoptosis (*7*). Treatment with hTF significantly reduced the level of cleaved RIP kinase by 76.1% ($P = 0.028$; Fig. 3H), increased the antiapoptotic protein Bcl2 by 83.3% ($P = 0.028$; Fig. 3I), and reduced the number of TUNEL-positive cells (Fig. 3J). As expected, LFt staining intensity was reduced (Fig. 3K), in parallel to the reduction of iron deposits in the retina. Exogenous hTF prevented the activation of resident macrophages/microglial cells (fig. S4A, CD68, arrowheads) and decreased Müller glial cell activation (fig. S4B, GFAP, arrows). The iron-induced oxidative stress markers 4-HNE and 8-HGN were also decreased with hTF treatment (fig. S4, C and D). Together, these results demonstrate that treatment with exogenous TF efficiently protects the retina from two types of iron-induced toxicity:

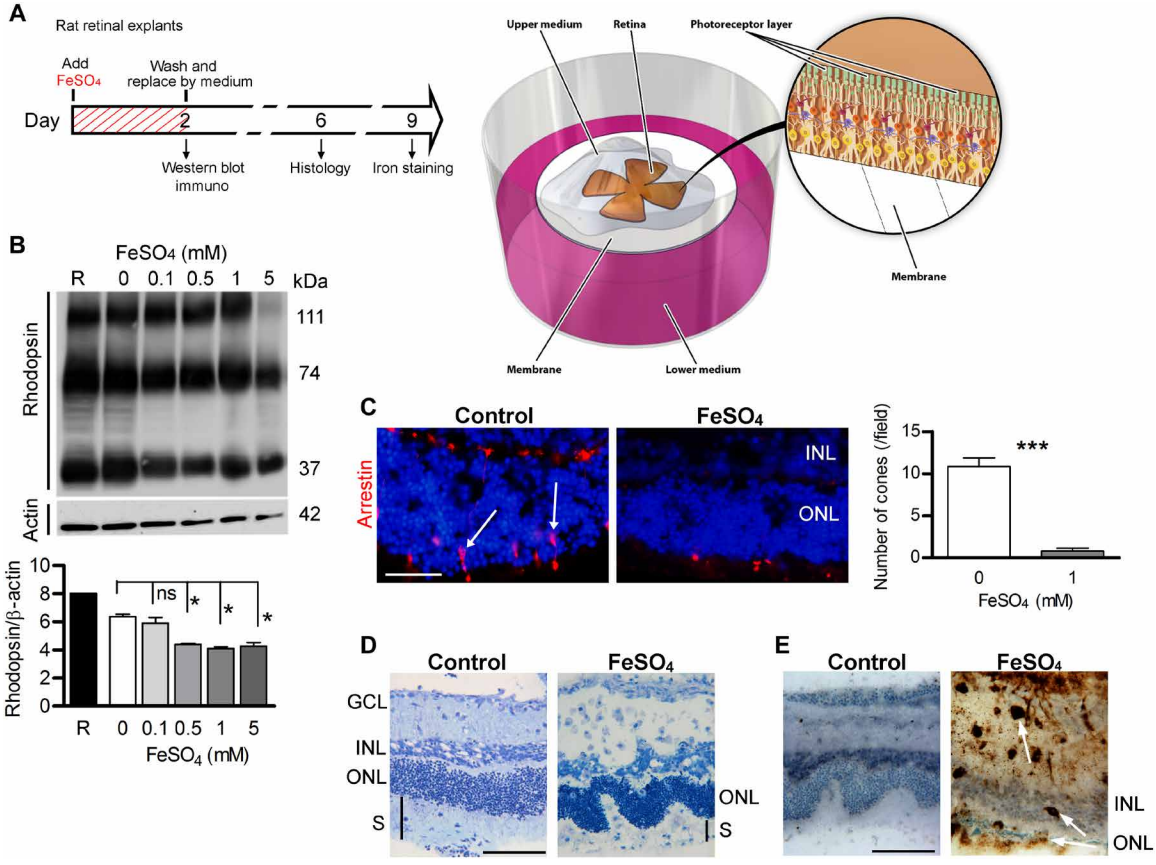

Fig. 2. Iron toxicity for PRs in rat retinal explants. (**A**) Illustration of the retinal explant model and the timed workflow for iron exposure protocol: Adult rat retinas were dissected, placed on membranes with PRs facing up, and immediately exposed for 2 days to iron ($FeSO_4$). Control explants were cultured with medium alone. Some explants were harvested, and Western blotting and immunostaining were performed. Afterward, the medium was completely replaced, and explants were maintained in culture for 4 or 7 days for histological analysis and iron staining, respectively. (**B**) Western blotting and quantitative analysis of a rod protein showed a decreased rhodopsin level in explants exposed to increasing concentrations of $FeSO_4$. The molecular masses of the immunolabeled fragments were indicated in the right margin. Mann-Whitney test ($n = 3$, $^*P = 0.028$). (**C**) Immunostaining of arrestin (red, arrows) and subsequent quantification showed very few cones present in explants exposed to 1 mM $FeSO_4$. Mann-Whitney test ($n = 3$, $^{***}P < 0.0001$). (**D**) Semithin sections of explants showed disorganization of the ONL and segments after 1 mM $FeSO_4$ exposure. (**E**) 3,3′-Diaminobenzidine (DAB) amplified Perl's reaction revealed iron deposits (arrows) in explants exposed to 1 mM $FeSO_4$. GCL, ganglion cell layer; ONL, outer nuclear layer; INL, inner nuclear layer; S, segments. Scale bars, 100 μm. All values are represented as the mean ± SEM.

direct and early necroptosis and delayed apoptosis that could result from secondary iron-related effects.

TF rescues the detached mouse retina in vivo

We induced partial RD in mice and rats (about 50 to 70% and 30 to 50% of the retinal surface, respectively). After 7 days, the detached retina was thickened, the outer nuclear layer (ONL) was disorganized, PR nuclei were pyknotic, OSs were absent, and RPE cells were enlarged in the detached area (fig. S5). Similar to human RD, iron accumulated in the detached rodent outer retinas (fig. S6, A and B) and in rat ocular fluids (52.54% increase in total iron levels after 14 days of detachment; $P = 0.042$) (fig. S6C). In TG mice (Fig. 4), hTF protected the detached retina from edematous thickening [21.7% decrease in retinal thickness of the detached retina/nondetached retina ($P = 0.045$), designated by brackets in Fig. 4A and quantified in the left graph of Fig. 4B] and from ONL thinning [20.3% decrease ($P = 0.033$); Fig. 4B, right graph] and prevented PR OS shortening [50% decrease ($P = 0.047$); graph in Fig. 4C and arrowheads in Fig. 4 (A and C)]. TG-detached retinas had 311.3% more cones than WT ($P = 0.025$; Fig. 4D). Activation of Müller glial cells was significantly reduced in TG mouse retinas (Fig. 4E, arrows). Compared with WT retinas, hTF expressed in TG retinas decreased *caspase 8* mRNA expression by 48.9% ($P = 0.008$), the level of the cleaved form of caspase 3 protein by 57.1% ($P = 0.03$), and the number of TUNEL-positive cells in the ONL of detached retinas by 56.3% ($P = 0.03$), demonstrating the antiapoptotic effect of TF in the mouse RD model (Fig. 4F). RIP kinase protein levels were reduced by 35.4% in the TG-detached retina compared with the WT ($P = 0.03$) (Fig. 4G), suggesting that hTF reduced both apoptotic and necrotic cell death in the mouse RD model.

Molecular signature of hTF overexpression in the mouse RD model

We performed a genome-wide analysis (RNA-seq) of neural retinas from TG and WT mice 4 days after induction of RD. From a total of 412 genes differentially regulated between TG and WT mice (1.5-fold change; $P \leq 0.05$), 149 were up-regulated and 263 were down-regulated. An extensive list is provided in data file S1. The 20 most up- and down-regulated genes are listed in table S1. Gene ontology (GO) (biological process, molecular function, and cellular compartment

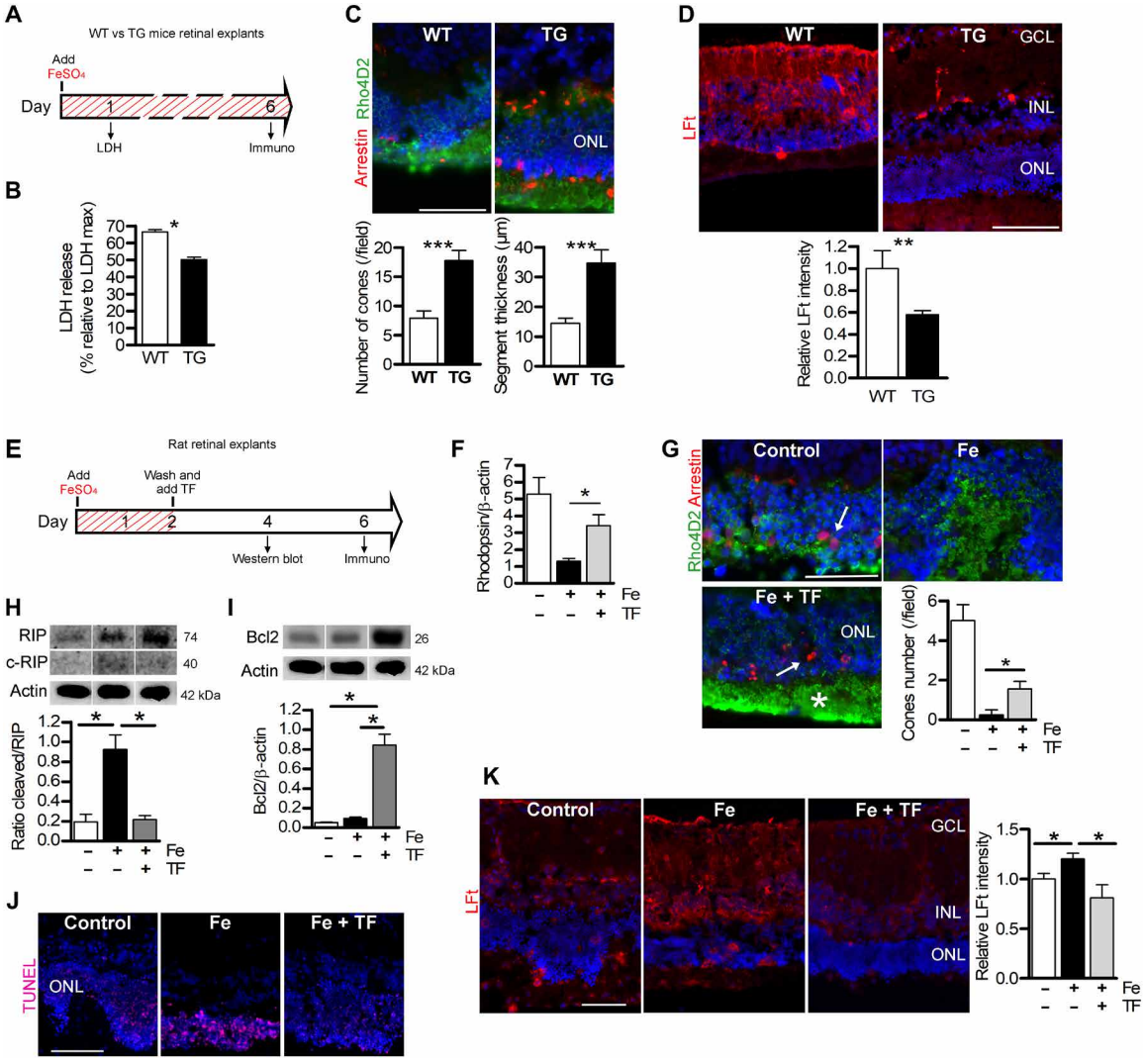

Fig. 3. Expression of TF protects retina explants exposed to iron. (**A**) Illustration of timed workflow for retinal explants from WT and TG mice expressing hTF continuously exposed to 1 mM $FeSO_4$. LDH release was measured after 1 day and immunostaining after 6 days. (**B**) LDH release was lower in culture medium from TG explanted mice compared to WT explants. Mann-Whitney test ($n = 6$), $^*P = 0.03$. (**C**) Number of cones stained by arrestin (arrow) and length of rod segments stained by rhodopsin (Rho4D2) were quantified and were higher in TG explants. Mann-Whitney test ($n = 3$), $^{***}P < 0.001$. (**D**) Quantification of immunostaining intensity for markers of iron storage LFt was decreased in TG explants compared with WT explants. Mann-Whitney test ($n = 3$), $^{**}P < 0.01$. (**E**) Illustration of timed workflow for TF treatment on iron-exposed explants: Adult rat retinas were exposed for 2 days with 1 mM $FeSO_4$. Control explants were cultured with medium alone. Afterward, the medium was completely replaced and explants were treated with hTF (50 mg/ml) for 2 or 4 days. (**F**) Quantitative analysis of rhodopsin protein by Western blotting show increased rhodopsin protein expression in TF-treated iron-exposed explants (Fe + TF). Mann-Whitney test ($n = 3$), $^*P = 0.021$. (**G**) Rhodopsin and arrestin immunostaining revealed protection of rod segments (Rho4D2, asterisk) and cones (arrow) by TF treatment (Fe + TF). Quantification of cone nuclei showed more cones in explants treated with TF than those exposed to $FeSO_4$. Mann-Whitney test ($n = 3$), $^*P = 0.036$. (**H**) Western blotting and quantitative analysis of RIP kinase demonstrated higher full form and cleaved form of the proteins in iron-exposed retinal explants. The cleaved form of RIP reported on RIP full form was reduced when TF was used to treat iron-exposed explants. Mann-Whitney test ($n = 3$), $^*P = 0.028$. (**I**) Antiapoptotic Bcl2 protein, detected by Western blotting, was increased in TF-treated iron-exposed explants. Mann-Whitney test ($n = 3$), $^*P = 0.028$. (**J**) TUNEL-positive cells in the ONL were reduced by TF treatment. (**K**) Immunostaining of iron storage marker ferritin light chain was significantly lower in explants treated with TF (Fe + TF) than without treatment (Fe). Fluorescence intensity was reported relative to control conditions. One-way analysis of variance (ANOVA), Bonferroni post test ($n = 3$), $^*P < 0.05$. Scale bars, 100 µm. All values are represented as mean ± SEM.

categories) and reactome pathway enrichment analysis demonstrated significantly affected categories in genes down-regulated or up-regulated in TG mice as compared with WT (Fig. 5; see data file S1 for details). We regrouped the significantly enriched pathways into 10 groups according to their biological functions: retina homeostasis, neurological process, phagocytosis, immune system, remodeling of extracellular matrix (ECM), mechanisms of cell death, metabolism, DNA/RNA regulation, intracellular signaling, and others, which comprise other biological functions such as cellular proliferation and differentiation (Fig. 5). The retina homeostasis group was solely composed with the most significantly enriched GO term "photoreceptor cell maintenance," which included genes related to the connector cilium linking the inner segment (IS) to the OS and playing a major role in rhodopsin transport toward OS disks. Pathways

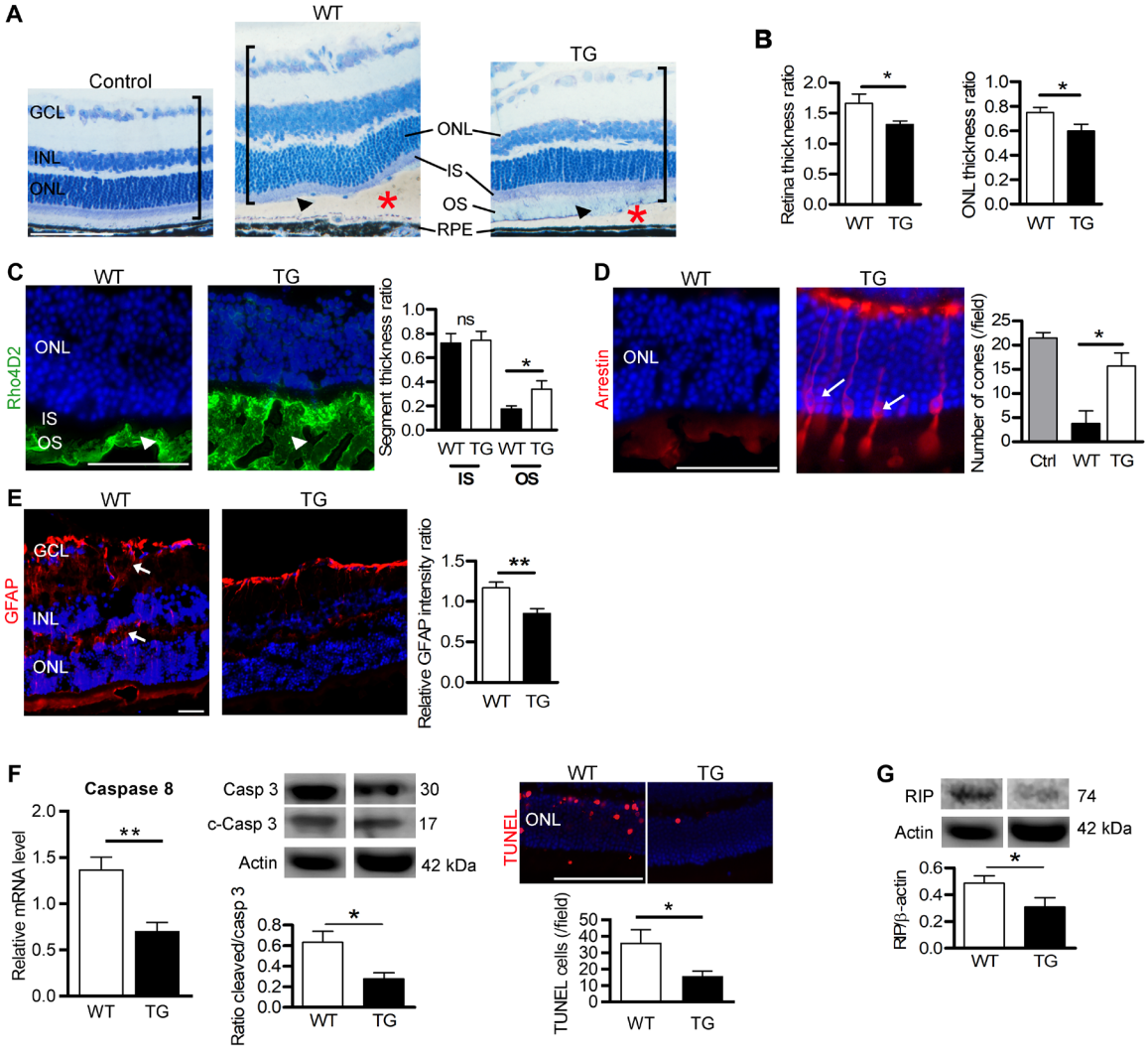

Fig. 4. TF expression preserves the detached retina in mice. (**A**) Semithin retinal sections from control WT mice without RD and WT and TG mice expressing hTF 7 days after RD (red asterisks). In TG mice, the histology of the detached retina (brackets) was less disrupted than in WT mice, with remaining OS (arrowheads). Nuclei were stained with toluidine blue. Measurements of total retinal thickness in the detached area were reported to undetached retina thickness. (**B**) Expression of hTF in mice (TG) reduced thickening of the total retina and ONL. Mann-Whitney test ($n = 5$), $^*P < 0.05$. (**C**) Rhodopsin staining in OS was conserved in TG compared with WT mice (arrowheads) 7 days after RD. The length of OS measured on semithin sections was higher in TG mice compared with WT mice. Mann-Whitney test ($n = 6$), $^*P = 0.047$ (**D**) Arrestin staining revealed cones in retinal sections of TG mice (arrows) 7 days after RD. Cone number was higher in TG compared with WT mice. Mann-Whitney test ($n = 6$), $^*P = 0.025$. (**E**) Müller glial cell activation revealed by GFAP expression was lower in TG mice compared with WT mice (arrows). Mann-Whitney test ($n = 5$), $^{**}P = 0.0056$. (**F**) Cellular markers of apoptosis were lower in TG compared to WT mouse retinas. Caspase 8 mRNA level by reverse transcription quantitative polymerase chain reaction (RT-qPCR), and the ratio of cleaved/pro–caspase 3 protein levels was determined by Western blotting performed 4 days after RD. TUNEL staining was performed in eyes collected 7 days after RD. Mann-Whitney test ($n = 5$), $^{**}P = 0.008$ and $^*P = 0.028$. (**G**) Necrotic RIP kinase protein level, detected by Western blotting, was reduced in TG mice compared with WT mice. Mann-Whitney test ($n = 3$), $^*P = 0.028$. IS, inner segment. Scale bars, 100 μm (A, E, and F) and 50 μm (C and D). All values are represented as the mean ± SEM.

relative to the neurological process group were especially involved in the regulation of neuron development and cognition. The phagocytosis group was composed of the most significant biological process according to the reactome analysis ("endoplasmic reticulum–phagosome pathway") that was also represented in GO analysis associated with the "receptor-mediated endocytosis" and the "regulation of vesicle fusion" pathways. The GO molecular function analysis revealed that "binding" was the most significantly enriched term (16 of a total of 29 terms) (data file S1). Furthermore, of the top 20 up- and down-regulated genes, half were associated with "protein binding" molecular function (GO term classification) (table S1). Pathways regrouped in the immune system group were also highly represented in the two enrichment analyses, and genes included in those were mostly up-regulated. Pathways related to the mechanism of cell death group were represented by two GO biological process terms involved in the regulation of apoptotic processes. In the 40 most significantly regulated genes, 12 were implied in cell death processes (table S1). The GO analysis of the cellular components showed 19 significant enrichments, which can be regrouped into three equal cellular compartments: the nucleus, the cytoplasm, and membranes (data file S1), reflecting cross-talk between the cell membrane and the nucleus.

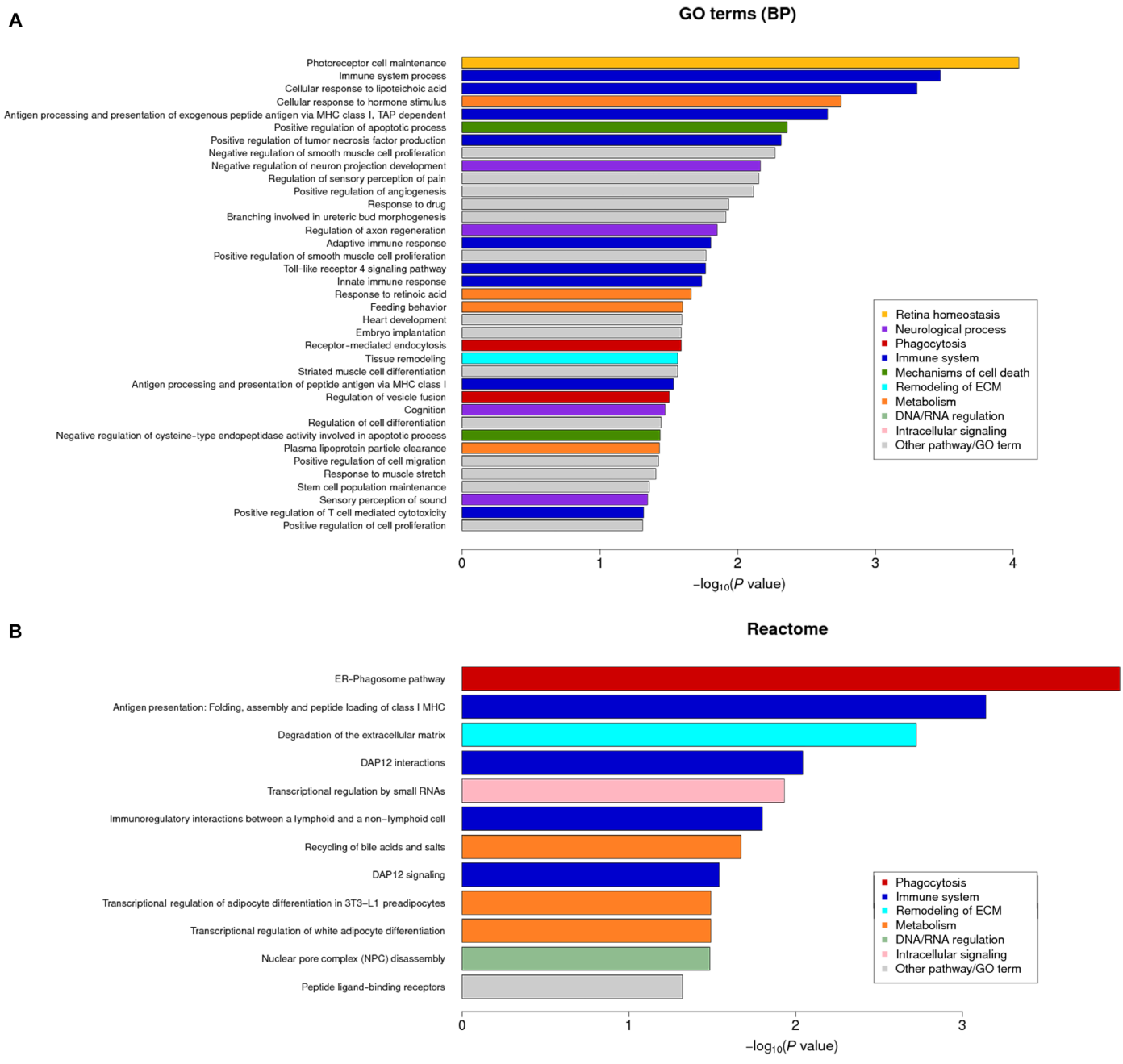

Fig. 5. High-throughput analyses of the transcriptome of TG mouse retinas following RD. Overrepresentation pathway analysis using GO terms enrichment (biological process clustering) (**A**) and reactome biosource (**B**). Color codes were used to associate pathways with common biological effects. Comparative analyses were carried out in TG versus WT retinas 4 days after RD ($n = 4$). GO terms and pathways were considered as enriched if fold enrichment is ≥2.0, uncorrected P value is ≤0.05, and the minimum number of regulated genes in pathway/term is ≥2.0. MHC, major histocompatibility complex; ER, endoplasmic reticulum.

Among the 412 genes differentially regulated between TG and WT mice, 2 genes (*Tfrc* and *Igfbp3*) encode proteins with direct interactions with TF (*17*). The insulin-like growth factor binding protein 3 (*Igfbp3*) transcript was significantly increased in TG mouse retina compared with WT 4 days after RD induction (fold change: 3.27, $P = 0.086$; table S1). In the normal retina, the IGFBP3 protein was localized in PR segments (arrowhead) in retinal capillaries and in the outer plexiform layer (arrow) (fig. S7A). Western blot analysis confirmed an increase of 46.7% of IGFBP3 protein level in the retinas of TG mice compared with WT mice 7 days after RD ($P = 0.028$; fig. S7B).

Local ocular injection of TF preserves detached rat retinas in vivo

In a therapeutic perspective trial, intravitreous injection of hTF (50 mg/ml) showed protective effects in a rat RD model (Fig. 6A). The retinal thickness of the detached retina/nondetached retina (Fig. 6A,

brackets, and Fig 6B, upper graph) was 14.2% lower in TF-treated rats ($P = 0.003$), whereas the ONL thickness was preserved [30.6% reduction ($P = 0.013$); Fig. 6B, middle graph], and immunostaining of rod and cone PRs (Fig. 6C) revealed preserved morphology. There was a 37.6% reduction of OS length (Fig. 6, B and C, arrowhead) in balanced salt solution (BSS) RD rats compared to TF-treated rats ($P = 0.004$; Fig. 6B, lower graph). Therapeutic TF thus reduced edema of the detached retina and preserved PR morphology. Together, these results indicate that TF, even if administrated at the time of RD, can prevent further retinal alterations and cell death.

DISCUSSION

Iron accumulation–induced oxidative stress has been observed in neurodegenerative and retinal diseases (*9*) and causes rapid PR death (*10*), but no correlation between intraocular iron and visual function has been demonstrated in a human disease. In our study, we show in human eyes increased iron levels and TSAT in the vitreous and SRF fluid, reflecting the accumulation of free iron in ocular tissues (RPE, PRs, and inflammatory cell–like) upon RD. Our results confirmed previous analyses that demonstrate increased oxidative stress in vitreous from patients with RRD (*18*).

Increased iron following RD could result from a combination of factors. In physiologic conditions, retinal iron entry is actively controlled through TF uptake by its receptor at the RPE basal membrane that forms the outer retinal barrier. After detachment, acute RPE alteration (*6*) may favor free iron entry. Similarly, a breakdown of the inner blood-retinal barrier in an animal model of type 2 macular telangiectasia, a rare human disease, led to iron accumulation in the retina and PR degeneration (*19*). However, iron accumulation was also shown in retinal dystrophies, especially in PRs, without obvious barrier breakdowns (*20*), suggesting that other mechanisms contribute to iron increases. PRs and RPE have high iron content because iron is a cofactor in phototransduction enzymes and have a major role in iron retinal homeostasis by the synthesis of TF (*20*). RPE cells, through the phagocytosis of shed OSs, recycle iron and export it from the retina (*20*). During RD, the loss of contact between PR and RPE leads to intracellular iron accumulation, a mechanism described in the Royal College of Surgeons (RCS) dystrophic rat, a genetic model of defective OS phagocytosis (*20*). PRs are extremely sensitive to iron excess, but the exact mechanisms of this toxicity have not been fully determined. We used organotypic retinal cultures to show that direct contact with iron causes rapid PR necrosis. Peroxidation by iron of polyunsaturated fatty acids in the OSs could be one necrotic mechanism (*21*). Furthermore, when iron has accumulated in the retina explant and after its removal from medium, apoptotic cell death observed could result from intracellular molecular iron-induced oxidation through the Fenton/Haber-Weiss reaction cycle (DNA, RNA, lipids, and proteins) (*9*), as suggested by DNA breaks (8-HGN) and lipid peroxidation (4-HNE) (fig. S4). Thus, labile iron exerts deleterious extracellular and delayed intracellular effects. The fact that vision recovery in patients with RRD was inversely correlated with ocular iron levels suggests that iron toxicity could be one of the mechanisms of PR loss over the time course of RRD.

The observed fully saturated TF in ocular fluids and intracellular iron accumulation in the retina suggest that iron loading capacities are saturated. Therefore, the use of TF appears as a relevant therapeutic therapy. Chemical chelators (deferiprone, deferoxamine, or deferasirox) have already been evaluated in neurogenerative diseases after systemic administration (*22*). However, long-term iron chelation therapy, routinely used for instance in beta-thalassemia and chronic iron overload diseases, negatively affects patient's quality of life and induced ocular toxicity, including cataracts, maculopathy, and optic neuritis (*23*, *24*). Thus, the use of these chemical chelators in patients with RD without systemic iron overload could be deleterious for the eye. Moreover, intraocular local administration of chemical iron chelators would require repeated intravitreal injections due to their short half-life (*25*). Such local administration might cause excessive intracellular iron depletion due to the high chelator-to-iron ratio.

On the basis of these findings, we proposed to use local ocular TF to neutralize iron toxicity. We previously showed that TF is safe for ocular use even at high doses and prevents iron accumulation in RPE and PRs, and that iron-loaded (holoTF) and iron-free TF egresses the retina through the TF receptor at the RPE apical side (*12*). Using various models of retinal degeneration, we have previously showed that apoTF has a neuroprotective effect (*12*, *13*), but involved mechanisms have not been yet fully elucidated. Here, using two RD models, we confirmed that apoTF efficiently removes iron and exerts antioxidant and neuroprotective effects. However, recent studies have demonstrated that the blockade of apoptosis or necroptosis was required to protect the detached retina (*7*). Using TG mice that express hTF in the retina or using therapeutic regimens with exogenous TF, we demonstrated that TF reduced both the direct iron-mediated necroptosis through RIP kinase down-regulation and the delayed iron-induced apoptosis.

The biological effects of TF, present at high concentration in the normal vitreous, are not limited to iron metabolism, and the neuroprotective properties of TF result from numerous targeted pathways. Lesnikov *et al.* (*26*) previously demonstrated that upon binding to TF receptor 2 (TFR2), TF protected against Fas-induced cell death via the mitochondrial pathway by reducing BID cleavage, inhibiting caspase 3 and caspase 9 activations, and up-regulating survival signals such as Bcl-xL. The retinal transcriptome of TG RD mice compared with WT RD mice highlighted seven major groups of pathways regulated by TF: phagocytosis, immune systems, retina homeostasis, neurological process, remodeling of the ECM, mechanisms of cell death, and metabolism. TF up-regulated the expression of receptors involved in endocytosis (*Cd36*, *Cd14*, and *Siglech*) and down-regulated the expression of vesicle trafficking inhibitors (*Tbc1d14*, *Evi5*, *Tbc1d30*, and *Usp6nl*). As a cargo protein, TF facilitates endocytosis/phagocytosis (*27*) and vesicle trafficking (*28*). Among the numerous pathways involved in neuroprotection regulated by TF (table S2), the IGFBP3 pathway is of particular interest. The up-regulation of IGFBP3 by TF was confirmed at the protein level, and fig. S8 illustrates IGFBP3 pathways and the genes in this pathway that were up-regulated (red underlined) or down-regulated (green underlined) by TF. The main role of IGFBP3 is to regulate the various functions of IGFs (*29*). When iron levels are high, TF forms complexes with IGFBP3 (*17*), preventing binding to its receptors and subsequent apoptosis and growth inhibition (*29*). IGFBP3-TF complex internalization allows IGFBP3 to be released to cellular organelles (*30*) and mediates neuroprotective effects (see fig. S8 for more details) (*29*, *31*, *32*).

From the analysis of ocular fluids of patients with RRD, we have demonstrated the oversaturation of TF and iron overload in a human ocular disease. Despite a high TF concentration in the vitreous, iron accumulates in the retina in other human diseases as observed in AMD (*10*); thus, TF oversaturation could be a general mechanism

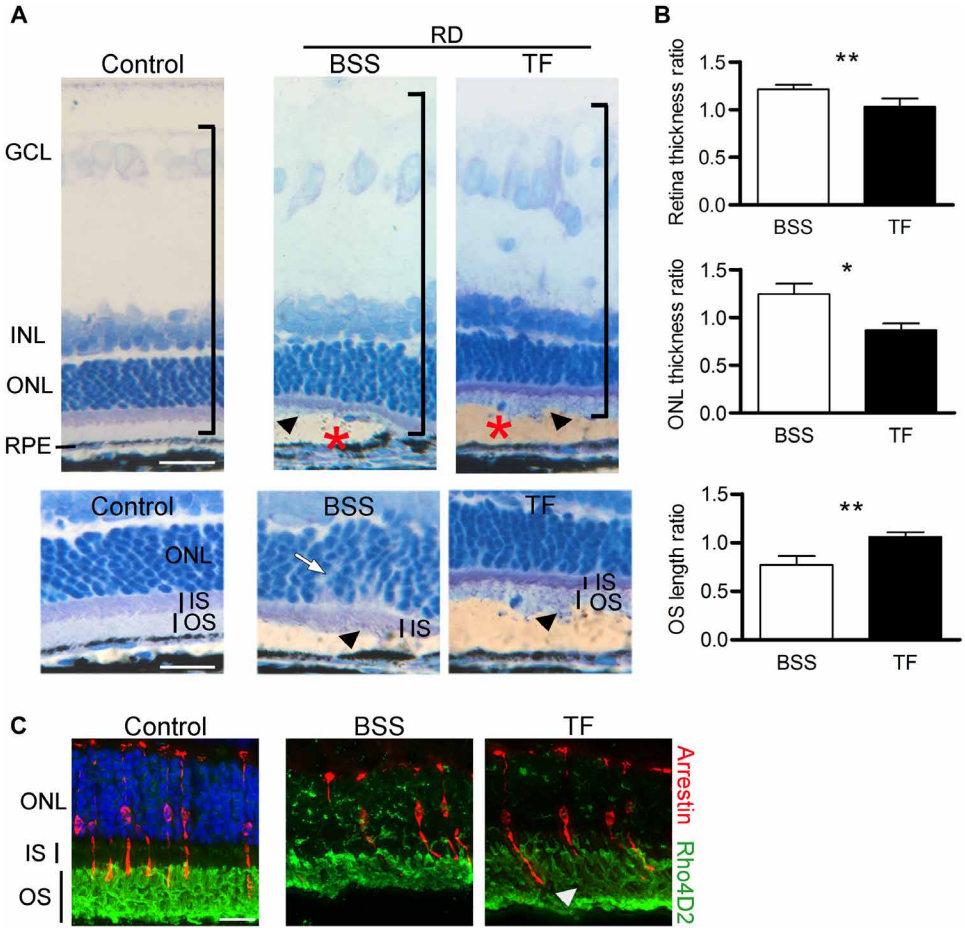

Fig. 6. Local administration of TF preserves neural retina in the rat model of RD. (**A**) Rat semithin retinal sections without RD (control) and with RD, treated by either intravitreal injection of a control solution [balanced salt solution (BSS)] or TF (50 mg/ml). Retinal histology in the detached area (asterisks) was more preserved in animals treated with TF compared with those receiving BSS. Higher magnifications showed less ONL disorganization (arrow) and longer OSs (arrowheads) in TF-treated RD rats. Nuclei were stained with toluidine blue. Measurements of thickness in detached retinas were reported relative to undetached retina thickness. (**B**) Treatment with TF reduced thickening of the total retina and the ONL. Mann-Whitney test ($n = 5$), $^{*}P = 0.013$ and $^{**}P \leq 0.01$. The length of OSs was higher in TF-injected RD rats. Mann-Whitney test ($n = 5$), $^{**}P = 0.007$. (**C**) Rhodopsin (green) and arrestin (red) staining in rats 7 days after RD. OSs were preserved in TF-treated animals (arrowhead). Scale bars, 20 μm (A and C) and 50 μm [(A) high magnification]. All values are represented as the mean ± SEM.

of PR cell death. Therefore, TF supplementation is a credible strategy for further translational clinical trials in eligible patients. As compared with other iron chelators, TF treatment not only restores iron homeostasis but also activates major neuroprotective pathways such as the IGFBP3 pathway. Future work elucidating the iron-unrelated pathways of TF will be required. We have used RD as a "model disease" in which neuroprotective treatments could show functional endpoints in a reasonable time frame. On the basis of the results obtained from experimental models and from human pathology and because TF is an endogenous molecule, clinical studies should be performed to evaluate TF in conjunction with RD surgery. Once validated, TF could be proposed as a treatment for other diseases associated with RD, such as in myopia, or those associated with iron overload such as AMD (*10*).

MATERIALS AND METHODS

Human samples

Consecutive patients presenting with RRD at Jules-Gonin Eye Hospital (Lausanne, Switzerland) from 1 December 2014 to 31 July 2015 were included according to the protocol approved by the ethics committee and diagnosed through normal standard clinical care at first examination. Upon presentation with RRD, the main inclusion criterion was the necessity of performing intraocular surgery to limit visual impairment in the absence of other ocular conditions. Among 44 vitreous samples, 35 samples were obtained from patients with macula-OFF RD. Nine sex-matched and age-matched patients presented with macular holes ($n = 4$) or with epiretinal membranes ($n = 5$), and no other ocular disease were included during the same period as control subjects for vitreous humor sampling.

Undiluted vitreous samples were collected by manual aspiration through a syringe connected to a 23-gauge vitrectomy cutter (before infusion opening; Alcon, Rotkreuz ZG, Switzerland). SRF was collected by active aspiration through a retinal tear (Advanced Backflush DSP cannula, Alcon, Rotkreuz ZG, Switzerland). Samples were coded and stored in a biobank at −80°C until biochemical analysis.

Duration of RRD (mean: 6.7 ± 5.9 days) was defined as the time from the onset of symptoms to surgery. Visual acuities were recorded before and 1 month after surgery and converted to the logarithm of

the minimum angle of resolution (LogMAR). Visual recovery was defined as the difference between postoperative and preoperative LogMAR visual acuity.

Frozen human postmortem eye tissues (10 donors) with nonhemorrhagic RD retrieved from the pathological files of Jules-Gonin Eye Pathology Laboratory were used to stain iron by Perl's method. A block of tissue (1 to 1.5 cm long and 0.5 cm wide) containing the RD was processed as serial 5-μm-thick paraffin sections.

Animals

Adult male Long-Evans rats (JANVIER LABS, Le Genest St Isle, France) (n = 32), adult male Wistar rats (JANVIER LABS) (n = 21), adult male C57BL6/J mice (WT) (JANVIER LABS) (n = 40), and adult male TG mice expressing human transferrin (TG) (Centre d'exploration fonctionnelle du Centre de Recherche des Cordeliers, UMRS1138, Paris France) (n = 40) were fed with a standard laboratory diet and ad libitum tap water in a room maintained at 21° to 23°C with a 12-hour light/12-hour dark cycle (6 a.m. to 6 p.m.). Mice were anesthetized with an intraperitoneal injection of ketamine (80 mg/kg; Virbac, Carros, France) and xylazine (12 mg/kg; Bayer, Lyon, France); rats were anesthetized with an intramuscular injection of ketamine (35 mg/kg) and xylazine (5 mg/kg). All animals were sacrificed by carbon dioxide inhalation.

Surgical induction of RD in rodents and study design

Features of retinal degeneration secondary to detachment were observed in animal models in which the retina is mechanically detached by the subretinal injection of sodium hyaluronate. Once anesthetized, Long-Evans rats or WT and TG mice received topical anesthesia with a drop of 1% tetracaine (Faure, Europhta Laboratories, Monaco). Pupil dilatation was achieved by dropwise instillation of 2 mg/0.4 ml mydriaticum (Théa Laboratories, Clermont-Ferrand, France) and 10% phenylephrine hydrochloride (Faure, Europhta Laboratories). RD was induced by a subretinal injection of 10 μl (mice) or 30 μl (rats) of sodium hyaluronate (5 mg/ml; Healon, Uppsala, Sweden) under an operating microscope using a 34-gauge needle through the sclera for a total of 50 animals. The induced RD occupied approximately 30 to 70% of the fundus. Eyes with hemorrhagic complications were excluded (nearly 15%). Eyes receiving no injection were used as controls.

Intravitreal injection in rats was performed immediately after RD induction with 5 μl of human apoTF solution (50 mg/ml in BSS; Sigma-Aldrich, Saint-Quentin en Yvelines, France) or control solution (BSS), as previously described (*12*).

Fundus and spectral domain optical coherence tomography were simultaneously realized with a Micron III retinal imaging microscope (Phoenix Research Labs, Pleasanton, CA, USA) in anesthetized animals as previously described (*12*) before and after RD induction and 4 or 7 days later. At 4 days, some mouse eyes were collected for RNA-seq (n = 4 eyes per group). At 7 days, eyes from rats and mice were collected for histology and immunostaining (n = 5 and 7 per group and per analysis for rats and mice, respectively). At 14 days, rat eyes (5 per group) were collected for assay of iron in ocular fluids.

Histology and thickness layer measurement

Fixed eyes were embedded in historesin (Leica, Nanterre, France) to facilitate the cutting of 5-μm-thick sections through the detached area. Sections were stained with 1% toluidine blue solution. Sections were observed on a Leitz microscope. Sections with the most detached retinal area were photographed (20×) with a Leica camera for measurements (n = 5 WT mice, n = 5 TG mice, n = 5 BSS-treated rats, and n = 5 TF-treated rats). Retinal thicknesses [from the OSs to the inner part of the ganglion cell layer (GCL) nuclei], the ONL, and the outer and inner segments were measured every 100 μm (mice) and 300 μm (rats) using ImageJ software by two different blind experimenters. Retinas were considered detached when an empty space was observed between the RPE and the OSs and attached when any signs of histological disturbance were observed. The retinal thickness ratio was calculated as the thickness in the detached retina/the thickness in the attached retina. For the ONL and segment thickness ratio, layer measurements were reported as the total retinal thickness of the corresponding retinal area using the formula (ONL detached/total retina detached)/(ONL attached/total retina attached).

Immunohistochemistry and fluorescence intensity evaluation

Fixed eyes were mounted in Tissue-Tek optimum cutting temperature (OCT) (Siemens Medical, Puteaux, France) to pass through the detached area. Explants were rinsed in 1× phosphate-buffered saline (PBS, Thermo Fisher Scientific, Cergy Pontoise, France), fixed for 20 min with 4% paraformaldehyde (Inland Europe, Conflans sur Lanterne, France), infiltrated in a sucrose gradient series, and then mounted in Tissue-Tek OCT. Immunohistochemistry was performed on 10-μm-thick sections as previously described (*12*). Primary antibodies were rabbit polyclonal anti-TFR1 (Serotec, Oxford, UK), rabbit polyclonal specific for the light subunit of ferritin (P. Santambrogio), rabbit anti-glial fibrillary acid protein (Dako, Thermo Fisher Scientific), rabbit anti-ionized calcium-binding adapter molecule 1 (Wako Pure Chemical Industries, Neuss, Germany), mouse anti-CD68 (Bio-Rad AbD Serotec GmbH, Colmar, France), anti–8-HGN (Abcam, Cambridge, UK), anti–4-HNE (Abcam), anti-rhodopsin (Rho4D2, Abcam), anti-cone arrestin (Millipore, Saint Quentin En Yvelines, France), and anti-IGFBP3 (Santa Cruz Biotechnology). Control sections were incubated with rabbit nonimmune serum (Thermo Fisher Scientific) or without primary antibodies. The corresponding Alexa-conjugated secondary antibodies (Thermo Fisher Scientific) were used to reveal the primary antibodies, and sections were counterstained with 4,6-diamidino-2-phenylindole (DAPI, Sigma-Aldrich). The TUNEL reaction was performed, along with DAPI staining, using the manufacturer's protocol (Roche Diagnostics, Meylan, France) as previously described (*12*). Propidium iodine (0.5 μg/ml) was incubated directly with sections for 1 hour, and the nuclei were counterstained with DAPI.

The sections were photographed with a fluorescence microscope (BX51, Olympus, Rungis, France) using identical exposure parameters for all compared samples. Blind quantifications were realized on photographs acquired at 40× magnification with ImageJ software as follows: Quantification of cone nuclei (arrestin staining) or TUNEL-positive cells (20× magnifications) in mouse (n = 5 per group) or rat (n = 5 per group) models of RD was performed using three photographs of the attached retina and three photographs of the detached retina. Measurement of the OS length in rat retina (n = 5 per group) was realized in six photographs by delimiting Rho4D2 staining and calculating the mean OS length in each retina area. The OS length ratio was then calculated as described for histological measurement. For the explant model, all quantifications were performed on four photographs (n = 3 explants per group). The OS length measurement was realized by measuring at three equidistant points on the

photographs. Fluorescence intensity staining was evaluated on photographs and reported as the mean intensity under control conditions. Each sample measurement was averaged, and differences between the groups were analyzed.

Retinal explant cultures

Adult Wistar rat retinas were isolated from fresh enucleated eyes, divided into four parts, and transferred to 0.2-mm polycarbonate membranes (Millipore) with the GCL facing the membrane (Fig. 2). Mouse retinal explants were isolated as indicated above, with one explant corresponding to one eye. The insert was placed into a six-well culture plate containing Dulbecco's modified Eagle's medium with L-glutamine and 5% serum (Thermo Fisher Scientific) corresponding to day 0. To analyze the effects of iron exposure on retinal explants, 30 µl of medium containing $FeSO_4$ ($7H_2O$; Sigma-Aldrich) was added to the PR side of the explants (upper chamber). To explore TF's therapeutic effects, the medium in the upper chamber was removed after 2 days. PBS was added for washing, and 30 µl of medium containing human apoTF (0.5, 5, or 50 mg/ml; Sigma-Aldrich) was placed on the retinas. LDH release and enzyme-linked immunosorbent assay (ELISA) directed against TF were measured in medium collected from the lower chamber as described previously (*12*, *13*). Histology, iron staining, immunohistochemistry, and Western blotting were performed on explants as described below and in the time workflow legends.

Iron status

Vitreous and SRF samples from humans, ocular fluids from RD rats, and medium from rat explants ($n = 6$ per group) were diluted with 1% HNO_3 solution containing Rh (10 ng/ml) and indium (10 ng/ml) as internal standards. In addition, each analytical batch of study samples was processed with laboratory controls, including method blanks and standard reference materials to continuously monitor method performance. Samples were analyzed using an ICP-MS (7700 Series, Agilent, Santa Clara, CA, USA). Quantitative analysis of iron (Fe) was carried out by external calibration using seven standards, with concentrations ranging from 10 to 1000 ng/ml. The method was assessed using internal and external quality controls, analysis of initial calibration, a verification standard, procedural blanks, and duplicate samples.

TF and proteins were quantified using an ELISA kit (AssayPro, St Charles, USA) and a Micro BCA assay kit (Thermo Fisher Scientific), respectively. For human samples, heme iron contamination was verified with a hemoglobin colorimetric assay (AssayPro). Saturation of TF was calculated as the total iron content (µM)/TIBC (µM). TIBC measures the amount of iron that can potentially be stored in TF and corresponds to the capacity of 1 mol of TF (80,000 Da) to bind 2 mol of ferric iron and was calculated (µM) as TF concentration (g/liter) $\times 10^6 \times$ (2/80,000).

Iron detection staining

Perl's reaction staining was performed by incubating in a solution containing 4% potassium ferrocyanide (Sigma-Aldrich) in 4% aqueous hydrochloric acid (Sigma-Aldrich) for 30 min at room temperature to yield a Prussian blue reaction product. Sensitivity for iron detection was enhanced by incubation with a solution of 3,3′-diaminobenzidine tetrahydrochloride (DAB, 5 mg/ml; Sigma-Aldrich) containing 1% H_2O_2 for 30 min at room temperature. For nucleus counterstaining, incubation with a solution of 1% nuclear red or toluidine blue (Sigma-Aldrich) was performed for 30 s. Stained sections were mounted in aqueous medium. Control of amplification was realized by incubation of sections with DAB without the preceding Perl's reaction step.

Imaging laser ablation (LA)–ICP-MS measurements were performed on a quadrupole instrument (Agilent 7700 ICP series, Darmstadt, Germany) hyphenated to a laser ablation system (NWR-213, New Wave, Fremont, USA) (*33*). Material on tissue sections was ablated by a Nd:YAG/213-nm laser focused at 18 µm diameter before transport toward the ICP ion source by a helium carrier gas with a flow rate of 800 ml/min. The LA-ICP-MS parameters were optimized to provide the best signal-to-noise ratio while keeping the maximum reproducibility between analyses. In this way, the energy output was set at 23%, corresponding to a laser fluency of 0.35 J/cm^2. The lateral resolution was fixed at 20 µm in the raster mode, with a scan speed and a repetition frequency of 20 Hz and 20 µm/s, respectively. $^{56}Fe^+$ was monitored for a duty cycle of 1 s. Raw data were acquired using MassHunter software (Agilent, Darmstadt, Germany). Data files (.d) of the Imaging MS (IMS) experiments were successively converted into mzML and imzML formats using msconvert and imzMLConverter tools, respectively. Ion images were reconstructed and visualized using the MSIReader v0.06 software.

Western blot analysis

Explants ($n = 4$ per group) were suspended in lysis MPER buffer (Thermo Fisher Scientific) and then centrifuged for 10 min at 4°C. Protein concentrations were calculated using the Micro BCA protein assay (Thermo Fisher Scientific). Five to 10 µg of total extract was mixed with protein loading buffer (Thermo Fisher Scientific) as per the manufacturer's instructions. Samples were loaded onto 4 to 12% bis-tris gel (Thermo Fisher Scientific), and proteins were transferred onto nitrocellulose membranes. Nonspecific binding was blocked with 5% nonfat dry milk in Tween/tris-buffered saline, and then membranes were incubated overnight at 4°C with the primary antibody against rhodopsin (1:5000; ab98887, Abcam), hTF (1:1000; ab88165, Abcam), IGFBP3 (clone E9, 1:1,000, Santa Cruz Biotechnology), caspase 3 (1:500; clone L-18, Santa Cruz Biotechnology), Bcl2 (1:500; clone N-19, Santa Cruz Biotechnology), RIP (1:500; clone 38, BD Transduction Laboratories), RIP3 (1:1000; PRS2283, Sigma-Aldrich), LC3B (1:1000; 2775, Cell Signaling Technology), or actin (1:4000; Sigma-Aldrich), followed by incubation with the supplier-recommended dilution of horseradish peroxidase–conjugated secondary antibody for 1 hour (Vector Laboratories, Eurobio, Les Ulis, France). Protein bands were visualized by an enhanced chemiluminescence reaction (Thermo Fisher Scientific) using a Bioimaging system (MicroChemi 4.2, Berthold, France). The gray values of specific bands were analyzed using ImageJ, and the protein signals of interest were reported relative to the actin signal or to their respective cleaved forms (for caspase 3 and RIP) for each sample.

Real-time reverse transcription polymerase chain reaction

Neural retinas were isolated on ice and directly frozen until RNA isolation. Tissues were homogenized in tubes prefilled with beads (Bertin Technologies, Ozyme, Saint Quentin en Yvelines, France) containing RLT lysis buffer (RNeasy mini kit, Qiagen, Courtaboeuf, France) for three cycles of 30 s at 5500 rpm in a Precellys Evolution homogenizer (Bertin Technologies, Ozyme, Saint Quentin en Yvelines, France). Total RNA was isolated with an RNeasy Mini kit (Qiagen, Courtaboeuf, France) according to the manufacturer's protocols. RNA concentration, purity, and integrity were determined with an Agilent Bioanalyzer.

All RNA used had an RNA integrity number (RIN) superior to 8. First-strand complementary DNA (cDNA) was generated by reverse transcription using 88 ng of total RNA and a QuantiTect Reverse Transcription Kit (Qiagen). Quantitative polymerase chain reaction (PCR) using duplicate technical replicates was performed on a QuantStudio 5 PCR System (Thermo Fisher Scientific) using SYBR Green gene expression assay probes (QuantiTect Primer Assay, Qiagen) of the mouse target genes caspase 8 (*Casp8*, NM_009812; QT00171437), *Igfbp3* (NM_0008343; QT00493332), an endogenous control actin b (*Actb*, NM_007393; QT01136772), and QuantiFast SYBR Green PCR Master Mix (Thermo Fisher Scientific). The expression levels of individual genes were normalized with *Actb* in the same sample by calculation of the ΔC_t value, and relative quantification was performed using the $\Delta\Delta C_t$ method with WT retina without DR serving as a control.

RNA sequencing

Retinas (n = 4 per group) were frozen immediately after isolation. Total RNA was extracted using a Precellys homogenizer (Ozyme, Bertin) and an RNeasy Mini kit (Qiagen). Samples were sent for sequencing to the iGenSeq transcriptomic platform of the Brain and Spine Institute (Paris, France). The RNA quality was evaluated by capillary electrophoresis (Agilent 2100 Bioanalyzer System), and RINs ranging from 7.8 to 8.2 were accepted for library generation. The cDNA library of each sample was prepared with a KAPA mRNA HyperPrep (Roche) for 75–base pair paired-end reads, according to the manufacturer's instructions. Each of the cDNA libraries was indexed for multiplexing (2 × 60 million reads per sample), and indexed libraries were sequenced on one lane of the Illumina NextSeq 500 device. Data were recorded in the FASTQ format.

RNA-seq data analysis

RNA-seq data analysis was performed by GenoSplice technology (www.genosplice.com). Sequencing, data quality, reads repartition (e.g., for potential ribosomal contamination), and insert size estimation were performed using FastQC, Picard Tools, SAMtools, and RSeQC. Reads were mapped using STAR v2.4.0 on the mm10 mouse genome assembly. A gene expression regulation study was performed as previously described (*34*). Briefly, for each gene present in the Mouse FAST DB v2016_1 annotations, reads aligning on constitutive regions (that are not prone to alternative splicing) were counted. On the basis of these read counts, normalization and differential gene expression were performed using DESeq2 on R (v.3.2.5). Only genes expressed in at least one of the two compared experimental conditions were further analyzed. Genes were considered as expressed if their reads per kilobase per million mapped reads (RPKM) value was greater than 93% of the background RPKM value on the basis of intergenic regions. Results were considered statistically significant for uncorrected P values ≤0.05 and fold changes ≥1.5 (GenBank accession number: GSE102824).

Pathway/GO analysis and transcription factor analysis

Clusterings and heat maps were performed on unlabeled data using "dist" and "hclust" functions in R, using Euclidean distance and the Ward agglomeration method. Analysis for enriched GO terms, KEGG pathways, and REACTOME pathways were performed using the Database for Annotation, Visualization and Integrated Discovery (DAVID) Functional Annotation Tool (v6.8). GO terms and pathways were considered enriched if the fold enrichment is ≥2.0, the uncorrected P value is ≤0.05, and the minimum number of regulated genes in the pathway/term is ≥2.0. Analysis was performed three times using all regulated genes, using up-regulated genes, and using down-regulated genes only. The union of these three analyses was performed to provide a single list of results. Analysis for transcription factors was performed using orthologous genes between the mouse and the human with the DAVID Functional Annotation Tool (v6.8). Orthologous genes are aggregated in FAST DB from Ensembl Compara. The same thresholds and methods as GO terms and pathway analysis were used but with human data.

Statistical analysis

Results are presented as the mean ± SEM. Analyses were performed using GraphPad Prism 5 software. Normal distribution of data was confirmed using the Shapiro-Wilk test. Comparisons between two groups of human ocular fluid samples were analyzed by an unpaired two-tailed Student's t test. Multiple comparisons were performed using one-way analysis of variance (ANOVA) followed by the Bonferroni post test as appropriate. Nonnormally distributed data were analyzed using a nonparametric Mann-Whitney test to compare the two groups. Unadjusted linear regression and two-tailed Pearson correlation analysis were performed to determine whether a relationship existed between iron concentration and delta LogMAR visual acuity or RD duration. $P < 0.05$ was considered statistically significant.

Study approval

The study involving human subjects adhered to the tenets of the Declaration of Helsinki and was approved by the local ethics committee of the Swiss Department of Health on research involving human subjects (CER-VD N°340/15). For vitreous and SRFs, written informed consent was obtained from all patients after detailed explanation of the purpose and methods of the study. All experimental procedures performed using rats and mice were approved by the local ethics committee of the Charles Darwin European Council, University of Paris-Descartes. Experiments were performed in accordance with the Association for Research in Vision and Ophthalmology statement for the use of animals in ophthalmic and vision research.

SUPPLEMENTARY MATERIALS

Supplementary material for this article is available at http://advances.sciencemag.org/cgi/content/full/5/1/eaau9940/DC1

Fig. S1. Cell death cellular markers in rat retinal explants exposed to iron.
Fig. S2. TF expression in mouse retinal explants protects from low-serum culturing conditions.
Fig. S3. TF expression in mouse retina explants reduced oxidative stress markers induced by iron.
Fig. S4. TF treatment preserves iron-exposed rat retinal explants from oxidative stress and inflammation.
Fig. S5. Animal models of RD.
Fig. S6. Iron accumulates in the rodent retina following RD.
Fig. S7. The expression of the TF protein partner, IGFBP3, in mice following RD.
Fig. S8. Proposed role of IGFBP3 in the protective effect of TF.
Table S1. Top 20 up- and down-regulated genes in TG compared with WT mice following RD.
Table S2. Pathways and genes regulated by TF and implicated in PR rescues.
Data file S1. Complete transcriptomic analysis.
References (*35*–*44*)

REFERENCES AND NOTES

1. Y. Murakami, S. Notomi, T. Hisatomi, T. Nakazawa, T. Ishibashi, J. W. Miller, D. G. Vavvas, Photoreceptor cell death and rescue in retinal detachment and degenerations. *Prog. Retin. Eye Res.* **37**, 114–140 (2013).
2. M. A. J. Van de Put, J. M. M. Hooymans, L. I. Los, Dutch Rhegmatogenous Retinal Detachment Study Group, The incidence of rhegmatogenous retinal detachment in The Netherlands. *Ophthalmology* **120**, 616–622 (2013).

3. B. A. Holden, T. R. Fricke, D. A. Wilson, M. Jong, K. S. Naidoo, P. Sankaridurg, T. Y. Wong, T. J. Naduvilath, S. Resnikoff, Global prevalence of myopia and high myopia and temporal trends from 2000 through 2050. *Ophthalmology* **123**, 1036–1042 (2016).
4. D. Mitry, M. A. Awan, S. Borooah, A. Syrogiannis, C. Lim-Fat, H. Campbell, A. F. Wright, B. W. Fleck, D. G. Charteris, D. Yorston, J. Singh, Long-term visual acuity and the duration of macular detachment: Findings from a prospective population-based study. *Br. J. Ophthalmol.* **97**, 149–152 (2013).
5. M. A. J. van de Put, L. Hoeksema, W. Wanders, I. M. Nolte, J. M. M. Hooymans, L. I. Los, Postoperative vision-related quality of life in macula-off rhegmatogenous retinal detachment patients and its relation to visual function. *PLOS ONE* **9**, e114489 (2014).
6. D. H. Anderson, W. H. Stern, S. K. Fisher, P. A. Erickson, G. A. Borgula, Retinal detachment in the cat: The pigment epithelial-photoreceptor interface. *Invest. Ophthalmol. Vis. Sci.* **24**, 906–926 (1983).
7. G. Trichonas, Y. Murakami, A. Thanos, Y. Morizane, M. Kayama, C. M. Debouck, T. Hisatomi, J. W. Miller, D. G. Vavvas, Receptor interacting protein kinases mediate retinal detachment-induced photoreceptor necrosis and compensate for inhibition of apoptosis. *Proc. Natl. Acad. Sci. U.S.A.* **107**, 21695–21700 (2010).
8. G. P. Lewis, C. J. Guérin, D. H. Anderson, B. Matsumoto, S. K. Fisher, Rapid changes in the expression of glial cell proteins caused by experimental retinal detachment. *Am. J. Ophthalmol.* **118**, 368–376 (1994).
9. R. Eid, N. T. T. Arab, M. T. Greenwood, Iron mediated toxicity and programmed cell death: A review and a re-examination of existing paradigms. *Biochim. Biophys. Acta* **1864**, 399–430 (2017).
10. X. He, P. Hahn, J. Iacovelli, R. Wong, C. King, R. Bhisitkul, M. Massaro-Giordano, J. L. Dunaief, Iron homeostasis and toxicity in retinal degeneration. *Prog. Retin. Eye Res.* **26**, 649–673 (2007).
11. E. Picard, I. Fontaine, L. Jonet, F. Guillou, F. Behar-Cohen, Y. Courtois, J.-C. Jeanny, The protective role of transferrin in Müller glial cells after iron-induced toxicity. *Mol. Vis.* **14**, 928–941 (2008).
12. E. Picard, Q. Le Rouzic, A. Oudar, M. Berdugo, M. El Sanharawi, C. Andrieu-Soler, M. C. Naud, L. Jonet, C. Latour, C. Klein, S. Galiacy, F. Malecaze, H. Coppin, M. P. Roth, J. C. Jeanny, Y. Courtois, F. Behar-Cohen, Targeting iron-mediated retinal degeneration by local delivery of transferrin. *Free Radic. Biol. Med.* **89**, 1105–1121 (2015).
13. E. Picard, L. Jonet, C. Sergeant, M.-H. Vesvres, F. Behar-Cohen, Y. Courtois, J.-C. Jeanny, Overexpressed or intraperitoneally injected human transferrin prevents photoreceptor degeneration in rd10 mice. *Mol. Vis.* **16**, 2612–2625 (2010).
14. J. Winkler, H. Hoerauf, The retinal organ culture—a model system for the examination of the early cytoskeletal reaction pattern after retinal detachment. *Klin. Monbl. Augenheilkd.* **225**, 269–275 (2008).
15. H. Matsumoto, J. W. Miller, D. G. Vavvas, Retinal detachment model in rodents by subretinal injection of sodium hyaluronate. *J. Vis. Exp.* **2013**, e50660 (2013).
16. G. P. Lewis, S. K. Fisher, Up-regulation of glial fibrillary acidic protein in response to retinal injury: Its potential role in glial remodeling and a comparison to vimentin expression. *Int. Rev. Cytol.* **230**, 263–290 (2003).
17. G. Miljuš, V. Malenković, B. Đukanović, N. Kolundžić, O. Nedić, IGFBP-3/transferrin/transferrin receptor 1 complexes as principal mediators of IGFBP-3 delivery to colon cells in non-cancer and cancer tissues. *Exp. Mol. Pathol.* **98**, 431–438 (2015).
18. M. Cederlund, F. Ghosh, K. Arnér, S. Andréasson, B. Åkerström, Vitreous levels of oxidative stress biomarkers and the radical-scavenger α_1-microglobulin/A1M in human rhegmatogenous retinal detachment. *Graefes Arch. Clin. Exp. Ophthalmol.* **251**, 725–732 (2013).
19. B. Baumann, J. Sterling, Y. Song, D. Song, M. Fruttiger, M. Gillies, W. Shen, J. L. Dunaief, Conditional Müller cell ablation leads to retinal iron accumulation. *Invest. Ophthalmol. Vis. Sci.* **58**, 4223–4234 (2017).
20. J. C. Jeanny, E. Picard, C. Sergeant, L. Jonet, M. Yefimova, Y. Courtois, Iron and regulatory proteins in the normal and pathological retina. *Bull. Acad. Natl. Med.* **197**, 661–674 (2013).
21. M. H. Guajardo, A. M. Terrasa, A. Catalá, Lipid–protein modifications during ascorbate-Fe^{2+} peroxidation of photoreceptor membranes: Protective effect of melatonin. *J. Pineal Res.* **41**, 201–210 (2006).
22. D. Devos, C. Moreau, J. C. Devedjian, J. Kluza, M. Petrault, C. Laloux, A. Jonneaux, G. Ryckewaert, G. Garçon, N. Rouaix, A. Duhamel, P. Jissendi, K. Dujardin, F. Auger, L. Ravasi, L. Hopes, G. Grolez, W. Firdaus, B. Sablonnière, I. Strubi-Vuillaume, N. Zahr, A. Destée, J. C. Corvol, D. Pöltl, M. Leist, C. Rose, L. Defebvre, P. Marchetti, Z. I. Cabantchik, R. Bordet, Targeting chelatable iron as a therapeutic modality in Parkinson's disease. *Antioxid. Redox Signal.* **21**, 195–210 (2014).
23. N. Parakh, R. Sharma, O. Prakash, D. Mahto, B. Dhingra, S. Sharma, J. Chandra, Neurological complications and cataract in a child with thalassemia major treated with deferiprone. *J. Pediatr. Hematol. Oncol.* **37**, e433–e434 (2015).
24. M. Di Nicola, G. Barteselli, L. Dell'Arti, R. Ratiglia, F. Viola, Functional and structural abnormalities in deferoxamine retinopathy: A review of the literature. *Biomed. Res. Int.* **2015**, 249617 (2015).
25. N. Mobarra, M. Shanaki, H. Ehteram, H. Nasiri, M. Sahmani, M. Saeidi, M. Goudarzi, H. Pourkarim, M. Azad, A review on iron chelators in treatment of iron overload syndromes. *Int. J. Hematol. Oncol. Stem Cell Res.* **10**, 239–247 (2016).
26. V. A. Lesnikov, M. P. Lesnikova, H. J. Deeg, Neuroimmunomodulation and aging: A role for transferrin and the hypothalamus/thymus axis. *Curr. Aging Sci.* **6**, 21–28 (2013).
27. H. Sakamoto, N. Sakamoto, M. Oryu, T. Kobayashi, Y. Ogawa, M. Ueno, M. Shinnou, A novel function of transferrin as a constituent of macromolecular activators of phagocytosis from platelets and their precursors. *Biochem. Biophys. Res. Commun.* **230**, 270–274 (1997).
28. A. Longatti, C. A. Lamb, M. Razi, S.-i. Yoshimura, F. A. Barr, S. A. Tooze, TBC1D14 regulates autophagosome formation via Rab11- and ULK1-positive recycling endosomes. *J. Cell Biol.* **197**, 659–675 (2012).
29. M. A. Johnson, S. M. Firth, IGFBP-3: A cell fate pivot in cancer and disease. *Growth Horm. IGF Res.* **24**, 164–173 (2014).
30. S. Storch, B. Kübler, S. Höning, M. Ackmann, J. Zapf, W. Blum, T. Braulke, Transferrin binds insulin-like growth factors and affects binding properties of insulin-like growth factor binding protein-3. *FEBS Lett.* **509**, 395–398 (2001).
31. R. C. Baxter, Nuclear actions of insulin-like growth factor binding protein-3. *Gene* **569**, 7–13 (2015).
32. K.-W. Lee, B. Liu, L. Ma, H. Li, P. Bang, H. P. Koeffler, P. Cohen, Cellular internalization of insulin-like growth factor binding protein-3: Distinct endocytic pathways facilitate re-uptake and nuclear localization. *J. Biol. Chem.* **279**, 469–476 (2003).
33. E. Lauer, M. Villa, M. Jotterand, R. Vilarino, M. Bollmann, K. Michaud, S. Grabherr, M. Augsburger, A. Thomas, Imaging mass spectrometry of elements in forensic cases by LA-ICP-MS. *Int. J. Leg. Med.* **131**, 497–500 (2017).
34. L. Noli, A. Capalbo, C. Ogilvie, Y. Khalaf, D. Ilic, Discordant growth of monozygotic twins starts at the blastocyst stage: A case study. *Stem Cell Rep.* **5**, 946–953 (2015).
35. D. Cosgrove, M. Zallocchi, Usher protein functions in hair cells and photoreceptors. *Int. J. Biochem. Cell Biol.* **46**, 80–89 (2014).
36. P. A. Williams, C. E. Braine, N. E. Foxworth, K. E. Cochran, S. W. M. John, GlyCAM1 negatively regulates monocyte entry into the optic nerve head and contributes to radiation-based protection in glaucoma. *J. Neuroinflammation* **14**, 93 (2017).
37. M. Gold, A. M. Dolga, J. Koepke, D. Mengel, C. Culmsee, R. Dodel, A. R. Koczulla, J.-P. Bach, α_1-Antitrypsin modulates microglial-mediated neuroinflammation and protects microglial cells from amyloid-β-induced toxicity. *J. Neuroinflammation* **11**, 165 (2014).
38. M. Lee, S. Li, K. Sato, M. Jin, Interphotoreceptor retinoid-binding protein mitigates cellular oxidative stress and mitochondrial dysfunction induced by all-*trans*-retinal. *Invest. Ophthalmol. Vis. Sci.* **57**, 1553–1562 (2016).
39. V. Higenell, E. S. Ruthazer, Layers upon layers: MHC class I acts in the retina to influence thalamic segregation. *Neuron* **65**, 439–441 (2010).
40. H. Matsumoto, K. Kataoka, P. Tsoka, K. M. Connor, J. W. Miller, D. G. Vavvas, Strain difference in photoreceptor cell death after retinal detachment in mice. *Invest. Ophthalmol. Vis. Sci.* **55**, 4165–4174 (2014).
41. C. R. Elliott-Hunt, F. E. Holmes, D. M. Hartley, S. Perez, E. J. Mufson, D. Wynick, Endogenous galanin protects mouse hippocampal neurons against amyloid toxicity in vitro via activation of galanin receptor-2. *J. Alzheimers Dis.* **25**, 455–462 (2011).
42. Y. Inoue, M. Shimazawa, S. Nakamura, T. Imamura, S. Sugitani, K. Tsuruma, H. Hara, Protective effects of placental growth factor on retinal neuronal cell damage. *J. Neurosci. Res.* **92**, 329–337 (2014).
43. A. S. Coyner, R. C. Ryals, C. A. Ku, C. M. Fischer, R. C. Patel, S. Datta, P. Yang, Y. Wen, R. Hen, M. E. Pennesi, Retinal neuroprotective effects of flibanserin, an FDA-approved dual serotonin receptor agonist-antagonist. *PLOS ONE* **11**, e0159776 (2016).
44. A. Maeda, T. Maeda, M. Golczak, Y. Imanishi, P. Leahy, R. Kubota, K. Palczewski, Effects of potent inhibitors of the retinoid cycle on visual function and photoreceptor protection from light damage in mice. *Mol. Pharmacol.* **70**, 1220–1229 (2006).

Acknowledgments: We thank Y. Courtois, A. Torriglia, I. Jaadane, and M. Abitbol (Centre de Recherche des Cordeliers, INSERM, UMRS 1138) for guidance, stimulating discussion, and manuscript reviews. We thank the Institut du cerveau et de la Moelle épinière (ICM) (Plateforme de Séquençage–iGenSeq; Hôpital de la Salpetrière) for RNA-seq and GenoSplice for data analysis. We wish to thank P. Santambrogio (Department of Biological and Technological Research, Instituto de Ricovero e Cure a Carattere Scientifico, San Rafaelle, Milan, Italy) for the rabbit polyclonal antibody specific for the high and light subunits of ferritin. We also wish to thank MSGraphique and S. Maroillez for illustrations. We would like to thank Editage (www.editage.com) for English language editing. **Funding:** This study was supported by INSERM, ANR JCJC 2015 Transfiron, The Abraham J. & Phyllis Katz Foundation, Veterans Administration RR&D Center Grant C9246C, Merit Award I01RX002806, SPiRE Award I21RX001924, NIH (R01EY028859 and P30EY006360), and an unrestricted grant from Research

to Prevent Blindness Inc. **Author contributions:** A.D. conducted experiments and surgeries, acquired and analyzed data, and wrote the manuscript. Q.L.R. conducted immunohistochemistry studies and PCR experiments and acquired data. L.J. conducted histological experiments. M.-C.N. conducted histological and animal experiments. L.K. acted as human samples biobank manager. J.-A.P. conducted surgeries and acquired data. J.H.B. conducted experiments, analyzed data, and wrote the manuscript. A.T. conducted iron assay experiments. N.T. conducted transferrin assay experiments. A.M. conducted human iron staining experiments. F.B.-C. designed research studies, conducted experiments, analyzed data, and wrote the manuscript. E.P. designed research studies, conducted experiments, acquired and analyzed data, and wrote the manuscript. **Competing interests:** The authors declare that they have no competing interests. **Data and materials availability:** All data needed to evaluate the conclusions in the paper are present in the paper and/or the Supplementary Materials. Additional data related to this paper may be requested from the authors. GenBank accession number: GSE102824.

Submitted 3 August 2018
Accepted 28 November 2018
Published 9 January 2019
10.1126/sciadv.aau9940

Citation: A. Daruich, Q. Le Rouzic, L. Jonet, M.-C. Naud, L. Kowalczuk, J.-A. Pournaras, J. H. Boatright, A. Thomas, N. Turck, A. Moulin, F. Behar-Cohen, E. Picard, Iron is neurotoxic in retinal detachment and transferrin confers neuroprotection. *Sci. Adv.* **5**, eaau9940 (2019).

Iron is neurotoxic in retinal detachment and transferrin confers neuroprotection

Alejandra DaruichQuentin Le RouzicLaurent JonetMarie-Christine NaudLaura KowalczukJean-Antoine PournarasJeffrey H. BoatrightAurélien ThomasNatacha TurckAlexandre MoulinFrancine Behar-CohenEmilie Picard

Sci. Adv., 5 (1), eaau9940. • DOI: 10.1126/sciadv.aau9940